

# Stick-like mesoporous titania loaded Pd as highly active and cost effective catalysts for hydrodebenzylation of hexabenzylhexaazaisowurtzitane (HBIW)

Shuang Liu<sup>a,1</sup>, Fei Ji<sup>a,1</sup>, Xiaoyu Li<sup>b</sup>, Xiaoli Pan<sup>b</sup>, Shuyuan Chen<sup>a</sup>, Xuefei Wang<sup>a</sup>, Yanhua Zhang<sup>c</sup>, Yong Men<sup>a,\*</sup>

<sup>a</sup> College of Chemistry and Chemical Engineering, Shanghai University of Engineering Science, Shanghai, 201620, China

<sup>b</sup> Dalian Institute of Chemical Physics, Chinese Academy of Sciences, Dalian, 116023, China

<sup>c</sup> Hebei University of Technology, Tianjin, 300401, China

## ARTICLE INFO

### Keywords:

Catalytic hydrogenolysis  
Debenzylation  
CL-20  
Pd catalyst  
Titania

## ABSTRACT

Hydrodebenzylation of hexabenzylhexaazaisowurtzitane (HBIW) is one key step for the synthesis of High Energy Density Compound CL-20 (hexanitrohexaazaisowurtzitane). Design of a “high atom economy” debenzilation catalyst to promote the industry production and massive use in the fields of aerospace and military has attracted great attentions. Herein, we designed a catalyst of stick-like mesoporous titania supported ultrafine Pd nanoparticles with low loading 2 wt.% using a hydrothermal and then deposition-precipitation method. The supports and catalysts were thoroughly characterized by N<sub>2</sub> physisorption, X-ray diffraction (XRD), scanning electron microscopy (SEM), high resolution transmission electron microscopy (HRTEM), Raman, ultraviolet–visible absorption (UV–vis), *in situ* diffuse reflectance infrared Fourier transform (DRIFT), H<sub>2</sub> chemisorption to determine their physical and chemical properties. The results revealed that stick-like titania (ST) treated at low temperature showed rutile crystalline structure, large interplanar spacing (3.2394 Å) and surface area (53 m<sup>2</sup>/g), small average crystallite size (63 nm) with mesoporous. The Pd can deposit into the interstices and lattice of ST and displayed ultrafine and even sub-nanometer sizes (average value 1.2 nm), and high dispersion. The Pd/ST-2 exhibited particularly high activity for hydrodebenzylation of HBIW. The product TADBIW was obtained in a high turnover number (TON) 107, which is 2–5 times higher than those of conventional Pd/C catalysts. This work paves a promising way to develop highly efficient catalysts with low loading of Pd and high atomic utilization for cost-effective synthesis of CL-20.

## 1. Introduction

Benzyl groups are often used to protect amine functionalities. The corresponding deprotection are significant fundamental transformations in multi-step organic syntheses. The most common method of deprotection is debenzilation under catalytic reduction conditions using H<sub>2</sub>. Heterogeneous Pd based catalysts are always massively applied in the process of debenzilation because of the advantages of good stability and easy separation [1–5]. Meanwhile they are often used also in the modern fine chemical industry [6–9]. However, low yield and large usage of precious metal catalyst limits mass production. The cost-effective processes are in urgent of development which can improve utilization of precious metal resource and reduce economic costs and

environmental pollution caused by post-treatment of the massive used Pd based catalysts. Meanwhile, the final deprotection in multi-step synthetic studies often fails because of an unanticipated poor yield, even if every required structural fragment is already constructed in the protected target molecular, which always troubles organic synthetic chemist. The catalysts play key roles to maximize product yield and minimize usage amount of noble metal. Developing high performance and economic catalysts for catalytic hydrodebenzylation has become a great challenge in the synthesis of complex organic compounds.

High Energy Density Compounds (HEDC) have so many versatile applications in the area of aerospace and arms and have attracted extensive attentions in recent years. Polycyclic nitramine hexanitrohexaazaisowurtzitane (HNIW, known as CL-20) is one of the most

\* Corresponding author.

E-mail address: [men@sues.edu.cn](mailto:men@sues.edu.cn) (Y. Men).

<sup>1</sup> As joint first-authors.

successful HEDC, which exhibits higher energy and density than common those of monocyclic nitramines, e.g., cyclotetramethylene tetranitramine (HMX) and cyclotrimethylene trinitramine (RDX) [10–12]. On the basis of the superior performances, it has become the key to break through the performances of the current propellants or explosives in specific impulse, burning rate, ballistic and detonation velocity. The industry synthesis of CL-20 includes four steps as shown in Scheme S1, Electronic Supporting Information (ESI) [12–18]. The conversion of the key intermediate hexabenzylhexaazaisowurtzitane (HBIW) to tetraacetyldibenzylhexaazaisowurtzitane (TADBIW) is the major challenge of the CL-20 synthesis due to not only multiplex reaction process but also the special features of HBIW [18–22]. The debenzilation of HBIW is a simultaneous hydrodebenzilation-acetylation process during which the C–N bonds are hydrogenolyzed on the catalysts followed by the acetylation of the forming amines with acetic anhydride. The removing of all benzyl groups is essential in the conditions including high temperature (30 °C–60 °C) and acid, such as acylation reagent acetic anhydride, solvent acetic acid, additive HBr from PhBr. However, HBIW has a complex molecular structure, which contains two five-membered rings with four N-benzilation groups and a six-membered ring with two N-benzilation groups, meanwhile, a C–C bond with high tension connects the two five-membered rings in the polycyclic caged organic compound. Due to the features, HBIW is unstable and decomposes easily in acid or heated conditions. In order to avoid destruction of the cage, the debenzilation needs to be launched and transformed quickly at low temperature (generally 15 °C–23 °C). The better starting temperature can be controlled at 17 °C–19 °C by a series of optimization experiments as shown in Scheme S2, ESI. The intermediate production DATBIW (diacetyltetrazabenzylhexaazaisowurtzitane) obtained by removing the two benzyls of HBIW can be more stable and endure higher temperatures than HBIW. To accelerate the debenzilation of DATBIW, the heating can be carried out with higher temperature (usually 34 °C–40 °C). In the current reports, high efficiency of the transformation has to be guaranteed by very large amount of noble metal, such as high loading of Pd, to supply enough active sites [12,19,20]. Commercial Pd/C catalyst with high Pd loading (5 wt.%–10 wt.%) is commonly used. However, the low atom utilization rate of Pd over the catalysts leads to high cost of synthesis and then limits the mass-production and widespread application of CL-20. Exploring industrial available catalysts with high efficiency and low loading of Pd, i.e., high atom economy, is urgently required for the hydrodebenzilation of HBIW.

Pd supported catalysts for debenzilation of HBIW focused on the use of different carbon carriers, e.g., various activated carbon, synthetic carbon [13,16,18,21,23,24]. It was discovered that target product can be hardly obtained when the loading of Pd was lower than 5 wt.% under constant usage amount of catalysts. Maksimowski et al. [19] prepared 10 wt.% Pd catalyst using Gryf-Skand Carbo Medicinalis active carbon as support and studied deactivation of the catalyst in HBIW hydrodebenzilation reaction. It was revealed that the aggregation of palladium particles occurred and then decreased the catalytic performance for debenzilation of HBIW. It is well known that gathering of Pd often emerges due to the weak interaction between the carbon and active metal. In order to make up for the loss of the active sites, more Pd needs to be provided. Hence, it is important to enhance the interaction between the support and Pd in order to stabilize the dispersion of Pd. In addition, in our previous study it was found that common carbon with the micropore (< 2 nm) as a carrier can form great Pd particles which showed low utilization rate of Pd for HBIW debenzilation while mesoporous carbon can reduce particle size of Pd and then improve the activity [25]. It can be inferred that the microporous structure of the common carbon support generated large Pd particles which reduced the number of the active center and decreased the atom economy. Therefore, it is important to enhance the pore structures of the support in order to upgrade the Pd atom utilization for HBIW debenzilation.

It is known that the mesoporous framework with 2 nm–50 nm pores

compared with the microporous structure (< 2 nm) can facilitate fast intraparticle molecular transfer of the substrate and product molecules and promote dispersion of active metal owing to large pore size, pore volume and high surface area [26–32]. On the basis of the advantages, the mesoporous catalytic system can be expected to enhance the catalytic performances and raise the atom utilization of the active metal. Besides, metal oxide as support is an effective way to increase the stability of active metal because of strong metal-support interaction and maintain high catalytic activity [33–40]. In our previous reports, it was found that the commercial titania P25 carried PdFe bimetal catalysts displayed good performance with the yield 76% in the transformation of HBIW [41]. In that work, the titania was nonporous and only maintained the activity on the basis of high loading (6.5 wt.%) of Pd. The atom economy of Pd is still low. In order to decrease loading of Pd and heighten the atom utilization, we developed a strategy for synthesizing ultrafine Pd nanoparticles with mesoporous titania (ST) as a support in the study. The Pd/ST carried only 2 wt.% Pd and displayed high turnover number (TON) which surpassed those of all the Pd based catalyst reported. This work demonstrates low loading Pd and high yield for debenzilation of HBIW and opens the possibility to develop highly effective Pd over mesoporous metal oxide for organic synthesis of CL-20 in the way of high atomic economy.

## 2. Experimental

### 2.1. Catalyst preparation

All reagents with A.R. grade were purchased and used without further purification. The titania supports were synthesized by a coprecipitation and then hydrothermal method according to the reports [42]. Typically, 0.55 mL  $\text{TiCl}_4$  was dropped on 10 g ice under stirring with 300 r/min, then 2 mL  $\text{SrCl}_4$  (2.5 M) was mixed for 10 min. 20 mL KOH (4 M) was added dropwise. After 10 min, the stirring speed increased to 500 r/min and continued for 20 min. The white slurry was obtained and transferred into 100 mL autoclave, which was sealed and heated at 100 °C for 24 h. After cooling, the product  $\text{SrTiO}_3$  was filtered, washed with distilled water for several times and dried at 70 °C for 4 h. 0.5 g  $\text{SrTiO}_3$  was put into 50 mL autoclave equipped with a Teflon liner, then 25 mL  $\text{H}_2\text{O}$  and 2.5 mL HCl was successively added into the autoclave. The autoclave was heated at 130 °C for 2.5 h under autogenous pressure and naturally cooled to room temperature. For the mixture taking from the autoclave, different treatment temperatures, freeze-drying, 60 °C heating and 120 °C heating, were carried out for 10 h. The corresponding powder finally received was marked as ST, ST(60) and ST(120). The sample T was prepared without  $\text{SrCl}_4$ , and all other steps were the same as ST.

Catalyst were synthesized through a deposition-precipitation (DP) method. In a typical preparation, 500 mg of ST was mixed with 100 mL of deionized water through a vigorous stirring to form a white suspension. Next, calculated  $\text{H}_2\text{PdCl}_4$  aqueous solution (10 mg Pd/mL, obtained by dissolving  $\text{PdCl}_2$  from STREM with HCl solution) was dripped into the suspension. The new suspension was continuously stirred for 3 h. The pH value of the mixture was then carefully adjusted to 9.5 by gradually introducing 10% NaOH solution, followed by vigorously stirring for another 5 h. The slurry was then filtered and washed. The filtrate was concentrated by a Rotary evaporator and then tested by Inductively Coupled Plasma Atomic Emission Spectrometry (ICP-AES, Varian 725-ES ICP). No Pd cation can be detected which indicated all input Pd cation was loaded on the ST support. The catalyst was dried at 60 °C in an oven overnight and termed as Pd/ST-x. x was designated as the loading of Pd, 1 wt.%, 1.5 wt.%, 2 wt.% and 2.5 wt.%. At the same time, Pd/ST(60)-2, Pd/ST(120)-2, and Pd/T-2 with 2 wt.% Pd loading were acquired by the same process. The actual loading of Pd was tested by ICP-AES.

## 2.2. Catalyst characterization

The nitrogen adsorption-desorption measurements were performed at  $-196\text{ }^{\circ}\text{C}$  with a Micromeritics ASAP 2460 instrument. Prior to the measurements, the samples were degassed at 298 K for 5 h. The specific surface areas were calculated with BET equation and the average pore diameters were estimated with desorption branches based on BJH model. Field emission scanning electron microscopy (FESEM) experiments were performed with a FEI Nova NanoSEM 450 electron microscope operating at 15 kV. The X-ray diffraction (XRD) patterns were recorded with a Bruker: D2 Phaser system, using Cu  $K\alpha$  monochromatized radiation ( $\lambda = 0.1541\text{ nm}$ ) combined with nickel filter at a scan speed of 0.5 s/step, 30 kV and 10 mA. Laser Raman spectroscopic measurements were performed on a Thermofisher DXR Raman microscope system (Thermofisher Scientific Company). High resolution transmission electron microscopy (HRTEM) images were recorded on a JEM-2100 F microscope, operating at an accelerating voltage of 200 kV. Aberration-corrected high-angle annular dark-field scanning transmission electron microscopy (HAADF-STEM) images were obtained on a JEOL JEM-ARM200 F equipped with a CEOS probe corrector. Ultraviolet-visible absorption spectroscopy (UV-vis) was studied by SHIMADZU UV-2450 to obtain the reflectance spectra of the powder over a range of 200 nm–1000 nm. In situ diffuse reflectance infrared Fourier transform (DRIFT) spectra were collected on a VERTEX 70 V infrared spectrometer equipped with a mercury cadmium telluride (MCT) detector at a resolution of  $4\text{ cm}^{-1}$ . The experiments were carried out in a high temperature reaction chamber (HVC-DRP-5, Harrick) equipped with ZnSe windows. Prior to the adsorption, the samples were pretreated with He at  $120\text{ }^{\circ}\text{C}$  for 30 min. After the temperature decreased to  $25\text{ }^{\circ}\text{C}$ , the background spectrum was collected using 64 scans. Then the 3 vol.% CO/He was introduced for 30 min to the samples. The spectra were obtained after purging for 30 min with He.  $\text{H}_2$  temperature-programmed reduction ( $\text{H}_2$ -TPR) was carried out on a Micromeritics Autochem II 2920 apparatus equipped with cold trap. 100 mg of a sample was loaded into a U-shape quartz reactor and purged with  $30\text{ mL min}^{-1}$  Ar at  $120\text{ }^{\circ}\text{C}$  for 1 h to remove adsorbed species. Then, after cooling to  $-50\text{ }^{\circ}\text{C}$ , the flowing gas was switched to a 10 vol.%  $\text{H}_2/\text{Ar}$ , and the catalyst was heated to  $900\text{ }^{\circ}\text{C}$  at a ramping rate of  $10\text{ }^{\circ}\text{C min}^{-1}$ . Dispersion of Pd were tested through  $\text{H}_2$  pulse chemisorption with Micromeritics, Auto Chem II 2920 instrument. The sample was pretreated at  $50\text{ }^{\circ}\text{C}$  for 1 h with 10 vol.%  $\text{H}_2/\text{Ar}$  and then the gas was transferred into Ar at  $60\text{ }^{\circ}\text{C}$  for 30 min. Finally, the  $\text{H}_2$  pulses were measured at  $50\text{ }^{\circ}\text{C}$  with 10 vol.%  $\text{H}_2/\text{Ar}$ .

## 2.3. Catalytic performance test

All chemicals, dimethyl formamide (DMF), acetic anhydride ( $\text{Ac}_2\text{O}$ ), bromobenzene (PhBr) and glacial acetic acid, were purchased and used as received. HBIW were synthesized by the cooperation factory.

The debenzoylation of HBIW was carried out in a low pressure reaction vessel (volume 150 mL) equipped with a water bath and heating magnetic stirrer (500 rpm–600 rpm). Catalytic experiments were performed according to a described procedure [25,41]. The reactants: 2.5 mL of DMF, 1.5 mL of  $\text{Ac}_2\text{O}$ , 0.02 mL of PhBr, 1.0 g of HBIW and 0.05 g of catalyst, were put into the reactor. Subsequently, the reactor was purged three times with hydrogen. The reaction was then stirred under 4 bar pressure of  $\text{H}_2$  at  $17\text{ }^{\circ}\text{C}$ – $19\text{ }^{\circ}\text{C}$  for 7 h and then  $34\text{ }^{\circ}\text{C}$  for 16 h. Filter and washing with ethanol for three times were carried out. The filter cake was dried in oven at  $40\text{ }^{\circ}\text{C}$  and the grey solids containing target product TADBIW and the catalysts can be obtained. The purity was analyzed by HPLC (ESI, Experimental).  $^1\text{H NMR}$  (400 MHz, DMSO)  $\delta$ : 7.39 (t,  $J = 41.2\text{ Hz}$ , 10 H), 6.92–6.02 (m, 2 H), 5.70–5.13 (m, 4 H), 4.27–3.77 (m, 4 H), 2.20–1.67 (m, 12 H) tested on the basis of Varian 400MR. Anal. Calcd. for TADBIW ( $\text{C}_{28}\text{H}_{32}\text{N}_6\text{O}_4$ ): C, 65.10; H, 6.24; N, 16.27. Found: C, 64.57; H, 6.25; N, 16.18 obtained by Elemental vario EL III. The yield was calculated according to the weight of the grey

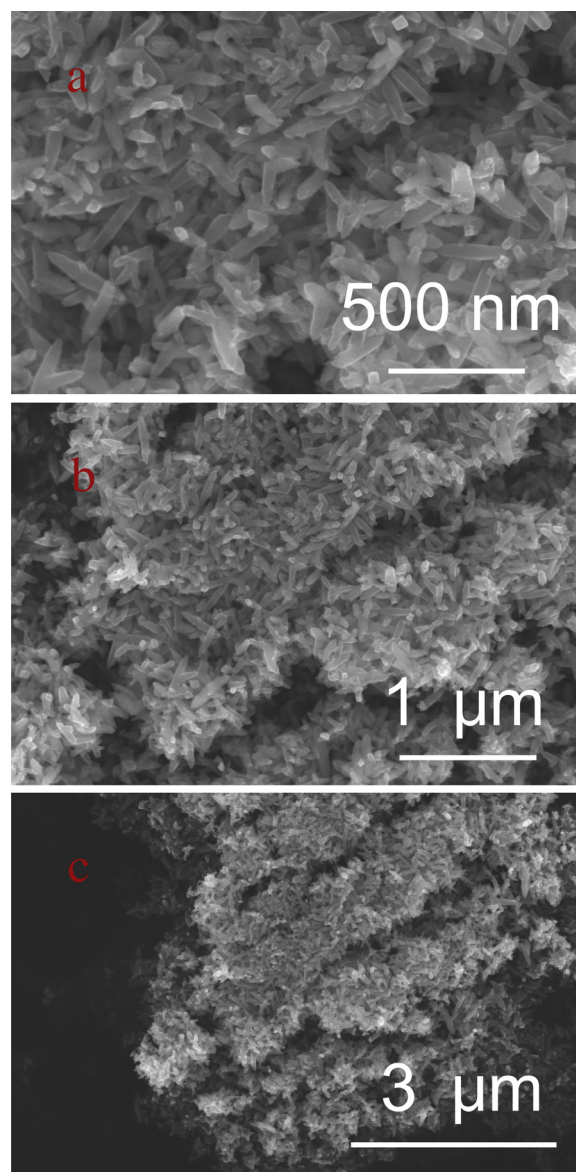


Fig. 1. FESEM pictures of the support ST at different scales (a–c).

solids subtracting that of the catalysts as reported [18,41].

$$\text{Yield} = \frac{(m_{\text{solid}} - m_{\text{cat}})}{m_{\text{HBIW}}} \times \frac{M_{\text{HBIW}}}{M_{\text{TADBIW}}} \times 100\%$$

TON can be calculated as follows:

$$\text{TON} = \frac{(m_{\text{solid}} - m_{\text{cat}}) \times P}{M_{\text{TADBIW}}} \times \frac{M_{\text{Pd}}}{m_{\text{cat}}L}$$

Here  $m_{\text{solid}}$ : the weight of the grey solid, g;  $m_{\text{HBIW}}$ : the weight of the reactant HBIW, g;  $m_{\text{cat}}$ : the usage of the catalysts, g;  $M_{\text{HBIW}}$  and  $M_{\text{TADBIW}}$ : the molecular weight of HBIW and TADBIW with 708.95 mol/g and 516.60 mol/g respectively;  $M_{\text{Pd}}$ : the atomic weight of Pd, 106.42 mol/g;  $P$ : the purity, %;  $L$ : the loading of Pd over the catalysts, %.

## 3. Results and discussion

### 3.1. Support characterization

FESEM of the support ST are shown in Fig. 1. It can be seen that ST was consist of a stick-like structure of  $\sim 20\text{ nm} \times 200\text{ nm}$ . According to the reports [42], these monodispersed titania NPs were formed via an

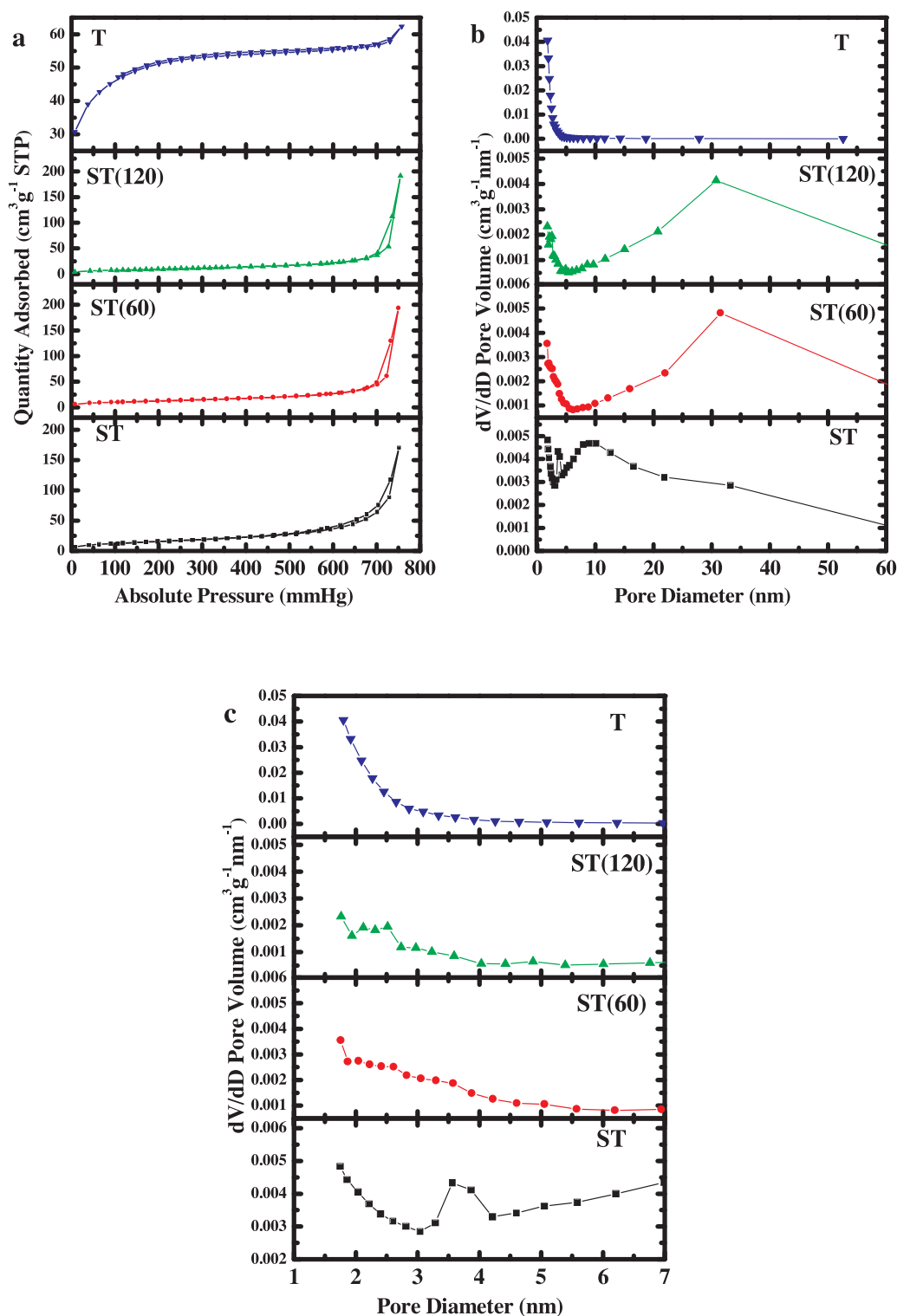


Fig. 2. a.  $\text{N}_2$  adsorption-desorption isotherms and the pore-size distributions of the supports (b. the whole ones and c. the enlarged ones).

oriented attachment (OA) mechanism and single crystalline was confirmed for each titania nanoparticle. Simultaneously, as shown in Fig. S1a-b, ESI, similar shape can be seen for the sample ST(60) and ST(120). However, the sample T exhibited a bulk structure, on the surface of which many grains like irregular NPs gathered in Fig. S1c, ESI.

Nitrogen adsorption-desorption isotherms of the supports, ST, ST(60), ST(120), T, together with the corresponding pore-size distributions are shown in Fig. 2. The specific surface area, and pore

volume of these supports are listed in Table 1. The isotherms of ST, ST(60) and ST(120) samples displayed type IV curves with a H3 hysteresis loop revealing a mesoporous structure, while the sample T showed the isotherms with type I curves due to microporous with the volume  $0.03 \text{ cm}^3/\text{g}$ . In addition, the sample T exhibited the largest surface area  $157 \text{ m}^2/\text{g}$ , the distribution of pore with less than 2 nm and  $0.06 \text{ cm}^3/\text{g}$  mesoporous volume. In contrast, ST, ST(60) and ST(120) showed no microporous volume, large mesoporous volume, uneven pore size and gradually decreasing surface area. The distribution of

**Table 1**  
Textural properties of the supports.

Sample	S <sub>BET</sub> <sup>a</sup> m <sup>2</sup> g <sup>-1</sup>	V <sub>micro</sub> <sup>b</sup> cm <sup>3</sup> g <sup>-1</sup>	V <sub>total</sub> <sup>b</sup> cm <sup>3</sup> g <sup>-1</sup>	average crystallite size <sup>c</sup> nm	interplanar spacing <sup>d</sup> Å
ST	53	0.00	0.11	63	3.2394
ST(60)	42	0.00	0.08	107	3.1960
ST(120)	32	0.00	0.06	116	3.1897
T	157	0.03	0.09	–	–

<sup>a</sup> surface area and.

<sup>b</sup> pore volume of pores was obtained by N<sub>2</sub> adsorption-desorption at –196 °C.

<sup>c</sup> average crystallite size determined by XRD analysis.

<sup>d</sup> calculated lattice constants from the strongest peak and crystal face (110).

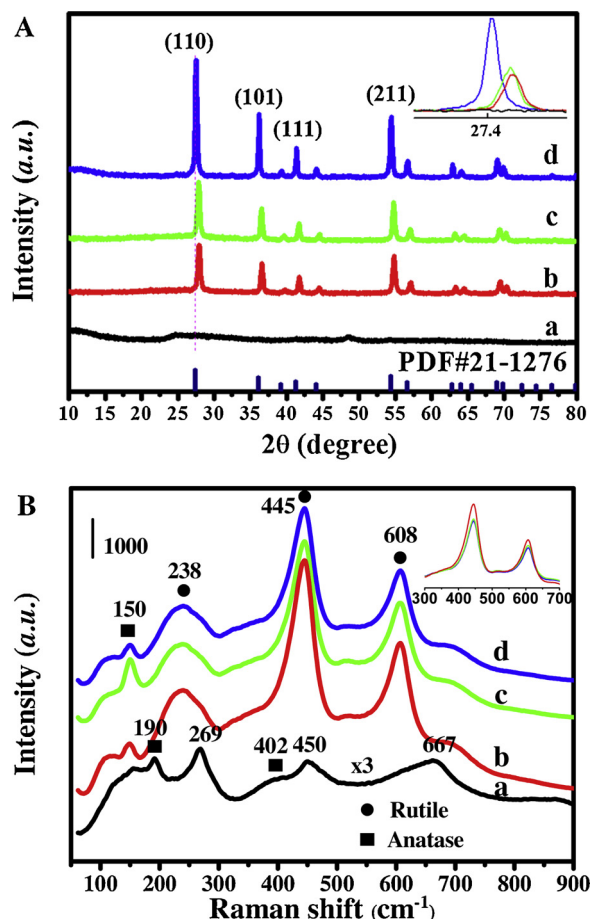


**Fig. 3.** A. XRD and B. Raman spectra of the supports a. T, b. ST(120), c. ST(60), d. ST.

pore focused on 3.6 nm and 10 nm for ST, and mainly centered on 32 nm for ST(60) and ST(120) which may be caused by crystal growing in the process of synthesis.

XRD tests were carried out. As shown in Fig. 3A, the sample T displayed no evident peak indicating amorphous morphology. Other samples exhibited the intense diffraction peak which can be ascribed to Rutile titania (PDF#21-1276). Noting that the peaks of the sample, ST, ST(60) and ST(120), with treatment temperature increase transferred to high angle shown as an inset in Fig. 3A, which may be caused by the interplanar spacing and average crystallite size. Then it can be calculated based on the strongest peak and crystal face (110) listed in Table 1. It can be found that the interplanar spacing decreased in the order of ST (3.2394 Å) > ST(60) (3.1960 Å) > ST(120) (3.1897 Å) while the average crystallite size according to Scherrer Equation grew

in sequence of ST (63 nm) < ST(60) (107 nm) < ST(120) (116 nm). It was indicated that ST supports showed larger interplanar spacing and smaller average crystallite size than others.

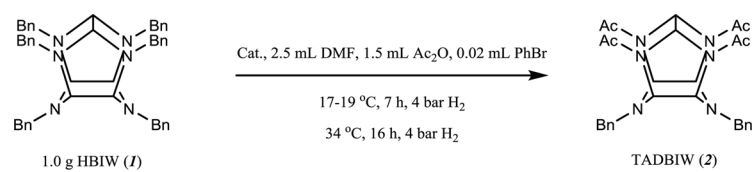
It is well known that the information depth of X-ray diffraction is on the order of tens of micrometers, while Raman scattering tends to provide information sensitive to the surface of the particles even in very small quantity. Raman spectra were measured and are shown in Fig. 3B in order to reveal and distinguish individual surface phases of titania. It can be seen that the sample T presented weak peak at 667, 450, 269, 190 cm<sup>-1</sup>. The peaks located at 450 and 190 cm<sup>-1</sup> can be attributed to the rutile and anatase phases of titania, respectively [43,44]. Jeon et al. [45] found that H<sub>2</sub>O<sub>2</sub> treatment can form Ti–OH on the surface of rutile titania corresponding to the peaks at 284, 531, and 691 cm<sup>-1</sup>. Considering that the sample T was obtained with hydrothermal processing and presented in amorphous morphology. It seems reasonable to conclude that Ti–OH could appear on the surface of the sample T as suggested by the Raman peaks at 667 and 269 cm<sup>-1</sup>. For ST, ST(60) and ST(120), four peaks (608 cm<sup>-1</sup>, 445 cm<sup>-1</sup>, 238 cm<sup>-1</sup>, 150 cm<sup>-1</sup>) emerged. Three typical vibrational modes around 608 cm<sup>-1</sup>, 445 cm<sup>-1</sup> and 238 cm<sup>-1</sup> were assigned as rutile titania, thereby confirming that the main titania crystal structure was rutile as revealed in XRD spectra; the weak peak at 150 cm<sup>-1</sup> maybe induced by seldom anatase phase of titania, and was attributed to O–TiO– bending type vibrations in accordance with the peaks as the reports [46]. Simultaneously, the gradually stronger broaden peaks could explain the growth of crystal size with increasing treatment temperature from ST to ST(120) well matching the discovery of XRD as shown in inset of Fig. 3B. On the basis of Raman scattering, it was suggested that the sample T contained the both anatase and rutile phase with Ti–OH on the surface although the bulk displayed amorphous morphology, while ST, ST(60) and ST(120) mainly exhibited rutile phase and revealed the little presence of anatase phase on the surface.

### 3.2. Catalytic performances

ST based catalyst with 2.5 wt.% Pd loading, Pd/ST-2.5, was studied for hydrodebenzylation of HBIW as shown in Table 2. The purity of the production TADBIW were detected by HPLC and listed in Table 2. As a contrast, commercial 10 wt.% Pd/C with 50 wt.% water from Degussa (marked as D-Pd/C) and 5 wt.% Pd/C from Sigma (marked as S-Pd/C) were investigated. The reaction introduced the same amount of dried catalysts independently of Pd loading. It can be observed that commercial D-Pd/C and S-Pd/C showed 76% and 74% yield with Pd/HBIW 5‰ and 2.5‰, respectively. Pd/ST-2.5 exhibited higher yield 82% and used less Pd/HBIW equal to 1.25‰ than those of the two commercial catalysts. High purity (92%–95%) for all TADBIW can be obtained. The addition of Pd over ST was further examined as presented in Table 2. For every hydrodebenzylation reaction, the feeding amount of catalysts was unchanged. As the loading of Pd decreased, the yield reduced from high yield to no production. It can be seen that high yield can be maintained when the loading of Pd was not lower than 2 wt.%.

On the basis of 2 wt.% loading, the other supports, ST(60), ST(120) and T, were tested and the results are listed in Table 2. No production appeared using the sample Pd/T-2. Pd/ST(60)-2 and Pd/ST(120)-2 showed low yield 73% and 57%. The catalytic performance in the reference currently reported are listed in Table 2. It was found that when loading of Pd decreased to 4 wt.%, no products can be obtained unless a large amount of catalysts were used [18,21,23]. For comparison, turnover number (TON) can be calculated by TADBIW products divided by input Pd. It was suggested that Pd/ST-2 catalysts showed the highest TON with 107 than common commercial D-Pd/C with TON 21 and S-Pd/C with TON 41 and all the reports listed in Table 2 including our previous work.

**Table 2**  
Catalytic performances for HBIW debenzylation over Pd based catalysts.



Entry	Sample	Loading of Pd <sup>c</sup> (wt.%)	Cat./HBIW (g/g)	Pd/HBIW (at.%)	Y <sub>TADBIW</sub> <sup>d</sup> (%)	TON <sup>e</sup> mol <sub>TADBIW</sub> /Pd	Purity <sup>f</sup> /[ref.] (%)
1	Pd/ST-2.5	2.1	0.05	7.0	82	111	95
2	D-Pd/C <sup>a</sup>	10.0	0.10	66.6	76	21	94
3	S-Pd/C <sup>b</sup>	5.0	0.05	16.6	74	41	92
4	Pd/ST-2	2.1	0.05	7.0	81	107	93
5	Pd/ST(60)-2	2.1	0.05	7.0	73	98	94
6	Pd/ST(120)-2	2.1	0.05	7.0	57	74	92
7	Pd/T-2	1.9	0.05	6.3	0	0	–
8	Pd/ST-1.5	1.4	0.05	4.6	31	61	93
9	Pd/ST-1	1.0	0.05	3.3	0	0	–
10	Pd(OH) <sub>2</sub> /C	20	0.02	26.6	86	28	87/ [24]
11	Pd/Sibunit C	10	0.10	66.6	86	12	–/ [23]
		6	0.10	40.0	82	20	
		4	0.1(0.2)	26.6(53.3)	0(76)	0(14)	
	Pd/CFC C	6	0.1	40.0	84	21	
12	Pearlman's Pd(OH) <sub>2</sub> /charcoal	20	0.25	333.1	63	1	–/ [12]
13	Degussa Pd/C	10	0.20	133.1	81	6	–/ [19]
	Pd/Carbo Medicinalis active carbon with H <sub>2</sub> O 50 %	10	0.20	66.6	79	11	
14	Synthesized palladium	13	0.20	173.2	73	4	–/ [16]
15	Pd(OH) <sub>2</sub> /C	10	–	26.6	92	33	96 [13]
			–	13.3	89	64	97/ [13]
16	Pd(OH) <sub>2</sub> /C	9	0.034	20.0	93	46	–/ [18]
		4.5	0.034	10.2	0	0	
17	Undried (< 50 % H <sub>2</sub> O) Pd(OH) <sub>2</sub> /C (Pearlman's)	20	1.01	–	35	–	94/ [20]
	Dried Pd(OH) <sub>2</sub> /C (Pearlman's)	20	0.51	679.5	33	0.4	89/ [20]
	Dried Degussa-type El01 NE/W	10	1.01	672.8	37	0.5	87/ [20]
			0.51	339.7	14	0.3	78/ [20]
18	Pd/Sibunit	6	0.10	40.0	82	20	–/ [21]
		10		66.6	86	12	
		4		26.6	0	0	
19	Pd/MC	10	0.10	66.6	80	12	–/ [25]
20	PdFeTi	6.57	0.03	13.1	76	57	99/ [41]

Commercial catalysts: <sup>a</sup> Degussa 10 wt.% Pd/C with 50 wt.% water; <sup>b</sup> Sigma 5 wt.% Pd/C; <sup>c</sup> obtained by ICP-AES. <sup>d</sup> separated yields; <sup>e</sup> calculated by TADBIW products divided input Pd; <sup>f</sup> tested by HPLC.

### 3.3. Catalysts characterization

With Pd deposited over ST, ST(60), ST(120) and T, no evident difference can be observed for the nitrogen adsorption-desorption isotherms given in Fig. S2a-S3a, ESI, but the obvious contraction can be revealed for total pore volume and surface area as displayed in Table 3. Noting that the microporous volume was still constant after supporting Pd over sample T. The pore-size distributions are showed in Fig. S2b-

**Table 3**  
Physical and chemical properties of Pd based catalysts with different supports.

Sample	Pd/ST-2	Pd/ST(60)-2	Pd/ST(120)-2	Pd/T-2
S <sub>BET</sub> <sup>a</sup> (m <sup>2</sup> g <sup>-1</sup> )	46	35	29	72
V <sub>micro</sub> <sup>b</sup> (cm <sup>3</sup> g <sup>-1</sup> )	0.00	0.00	0.00	0.03
V <sub>total</sub> <sup>b</sup> (cm <sup>3</sup> g <sup>-1</sup> )	0.10	0.06	0.05	0.05
H <sub>2</sub> pulse chemisorption <sup>c</sup> (cm <sup>3</sup> g <sup>-1</sup> )	1.85	1.53	1.41	0.98
Dispersion of Pd <sup>d</sup> (%)	88	73	67	47

<sup>a</sup> surface area and.

<sup>b</sup> pore volume of pores less than 403.122 Å diameter at P/Po = 0.95 was obtained by N<sub>2</sub> adsorption-desorption at – 196 °C.

<sup>c</sup> H<sub>2</sub> pulse chemisorption.

<sup>d</sup> based on the H<sub>2</sub> pulse chemisorption and input of Pd in the process of catalysts preparation.

S3b, ESI and the enlarged ones in Fig. 4a-b. The pore focused on 3.6 nm was changed. Specifically, the 3.6 nm pore disappeared with Pd loading increased over ST (Fig. 4b). It can be suggested that the introduction of Pd reduced the surface area and mesoporous volume, meanwhile the microporous volume seemed unchanged, which implied that Pd can precipitate preferentially in the edge or tunnel of the mesoporous structure over the support.

XRD of the catalysts with different loading and supports are shown in Fig. S5a-b, ESI. In all cases, the spectra were similar to those of the supports, *i.e.*, the XRD results did not demonstrate the appearance of any crystalline Pd phase. It was suggested that loading Pd nanoparticles to the supports formed either amorphous or small nanoparticles which goes beyond the detection of XRD.

TEM and HAADF-STEM pictures of Pd/ST-2 catalyst are showed in Fig. 5A-B and Fig. 5C respectively. It can be seen that ultrasml Pd NPs (≤ 2 nm) and even sub-nanometer clusters (< 1 nm) can be formed as a predominant presence and finely dispersed on the supports ST with average diameter 1.21 nm. Meanwhile, it can be revealed that the support ST was composed of dispersed titania NPs which was a stick-like crystal with many channels and mesoporous combined with nitrogen physical adsorption tests. Similarly, HAADF-STEM images of Pd based catalysts over ST(120) and T were displayed in Fig. 5D and E. It can be observed that ST(120) as supports exhibited slightly increased particles size with mean diameter 1.28 nm. In contrast, Pd particles obviously grew in the support T with average particle size 1.86 nm. It

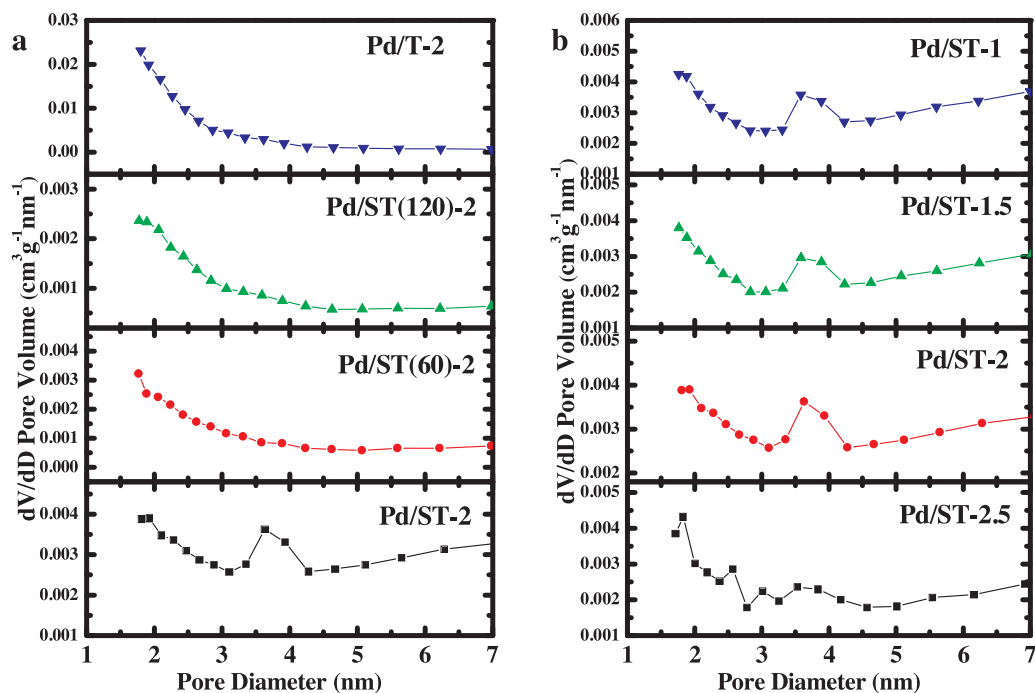


Fig. 4. Pore-size distributions of a. Pd deposited over different supports and b. ST based catalysts with different Pd loading.

can be seen that particle size of Pd increased over the supports as follows: ST < ST(120) < T which was consistent with HBIW debenylation.

ST supported Pd catalyst (Pd/ST-2) was further analyzed by HRTEM as shown in Fig. 6. The Pd was revealed to spread over the titania surface as a thin layer with amorphism about 1 nm thick. Combined with the preparation method of DP, it was indicated that the deposited Pd could be amorphous. Noting that the interjunctions were composed of fragmental lattice and variegated amorphous phase. In the area of supports without Pd particles, a lattice fringe of 0.242 nm can be ascribed to the (210) plane of titania. For the fields of Pd appeared, the enlarged lattice spaces can be clearly observed with 0.248 nm, 0.249 nm and 0.257 nm in Fig. 6a, b and c. In addition, evident lattice distortion can be observed in red frame of Fig. 6c. XPS spectra of the catalyst Pd/ST-2 were measured and are shown in Fig. S6, ESI. As a comparison, the XPS spectra of the catalysts Pd/ST(120)-2 and Pd/T-2 are given in Fig S6, ESI. The binding energy (BE) followed the order: Pd/ST-2 > Pd/ST(120)-2 > Pd/T-2 for Pd 3d while Pd/ST-2 < Pd/ST(120)-2 < Pd/T-2 for O 1s. The binding energy of Ti 2p unchanged over the three samples. The shift of Pd 3d to higher BE positions suggested the presence of electron-deficient Pd species ( $\text{Pd}^{\text{n}+}$ ) for Pd/ST-2. At the same time, the shift of O 1s to low BE positions implied low concentration of surface species on the Pd/ST-2. It is well known that  $\text{Ti}^{4+}$  (0.605 Å),  $\text{Pd}^{4+}$  (0.615 Å) and  $\text{Pd}^{2+}$  (0.640 Å) have approximative ionic radii [47]. It was reported that Pd can occupy interstices and then distort the titania lattice [48]. Meanwhile it was proposed that the nanocrystalline anatase and rutile had high surface energy and easily released deformation of phase accompanying grain boundary sliding and nanoscale cavitation [49,50], besides, pH and metal salt precursor can promote salt-support interaction [51] and the lattice of titania can be doped by Pd under a certain content [48]. Thus it can be inferred that in the initial process of DP, metal Pd produced a strong interaction with unstable edge and tunnel surface of titania, and then led to initial Pd penetrated into interstices even lattice by pH and the strong salt-support interaction. Subsequently sub-nanometer clusters and ultrafine NPs arisen.

UV-vis absorption spectra of ST, ST(120), T and corresponded Pd catalysts with theoretical 2.0 wt.% loading are presented in Fig. 7. Pd/

ST-2, Pd/ST(120)-2 and Pd/T-2 markedly showed the absorption spectra in the whole region compared with ST, ST(120) and T, which could be ascribed to deposit Pd. Meanwhile the intensity of the absorption peak became stronger for Pd/T-2 than Pd/ST-2 ~ Pd/ST(120)-2 in the visible region. For the ultraviolet region, the absorbance peak followed the order of Pd/ST-2 < Pd/ST(120)-2 < Pd/T-2. It was reported that the extinction spectra were red-shifted with increasing particle diameter of Pd [52]. The gradually grew Pd clusters were responsible for the strong absorption in the visible and ultraviolet region, which was consistent with the statistics obtained by HAADF-STEM.

Fig. 8 presents the Raman spectrum of Pd based catalysts recorded in the range of  $50\text{ cm}^{-1}$ – $1000\text{ cm}^{-1}$ . For the sample T, after Pd deposited, the peak at  $192\text{ cm}^{-1}$  of anatase phase,  $452\text{ cm}^{-1}$  and  $663\text{ cm}^{-1}$  of rutile phase disappeared as shown in Fig. 8a. Compared with the supports, the peak at  $150\text{ cm}^{-1}$  designated as anatase phase gradually became weaker for Pd/ST-2 and Pd/ST(120)-2. Weaken or even disappeared peaks can be contributed to Pd particles covered on the surface or phase transformation. Meanwhile the peak at  $445\text{ cm}^{-1}$  ascribed to rutile phase contained redshift for loaded Pd catalysts Pd/ST-2 and Pd/ST(120)-2 as revealed in Fig. 8b, nevertheless the supports ST and ST(120) displayed the same peak shift in Fig. 3B of Raman spectra. The shifting of the spectral peaks was demonstrated relative to the oxygen stoichiometry [43]. According to redshift of the main peak, it can be inferred that Pd precipitation induced the forming of oxygen defects for Pd/ST-2 and Pd/ST(120)-2 in consistent with O 1s of XPS. As implied by HRTEM and XPS, Pd deposited into the crystal interstices and lattice of surface, and then can produce oxygen defects. Similarly, Resasco et al. found that oxygen vacancies can be formed in Pd loaded titania system [53]. Meanwhile it was reported that in the DP method, because of better salt-support interaction, electron transfer would be more facile from Pd to titania surface and consequently the electron deficient Pd ( $\text{Pd}^{\text{n}+}$ ) species can be generated [51]. Thus it can be inferred that Pd/ST-2 can emerge the palladium–titanate species ( $\text{Pd}^{\text{n}+}$ -oxygen vacancy ( $\text{Vo}$ )- $\text{Ti}^{3+}$ ). ST(120) shaped better crystal structure than ST as obtained by XRD and then facilitate Pd deposited into the support, which was consistent with more Raman red shift of the main peak. By comparison, the support T had amorphous structure and then generated the disappearance rather than red or blue shift of the peaks.

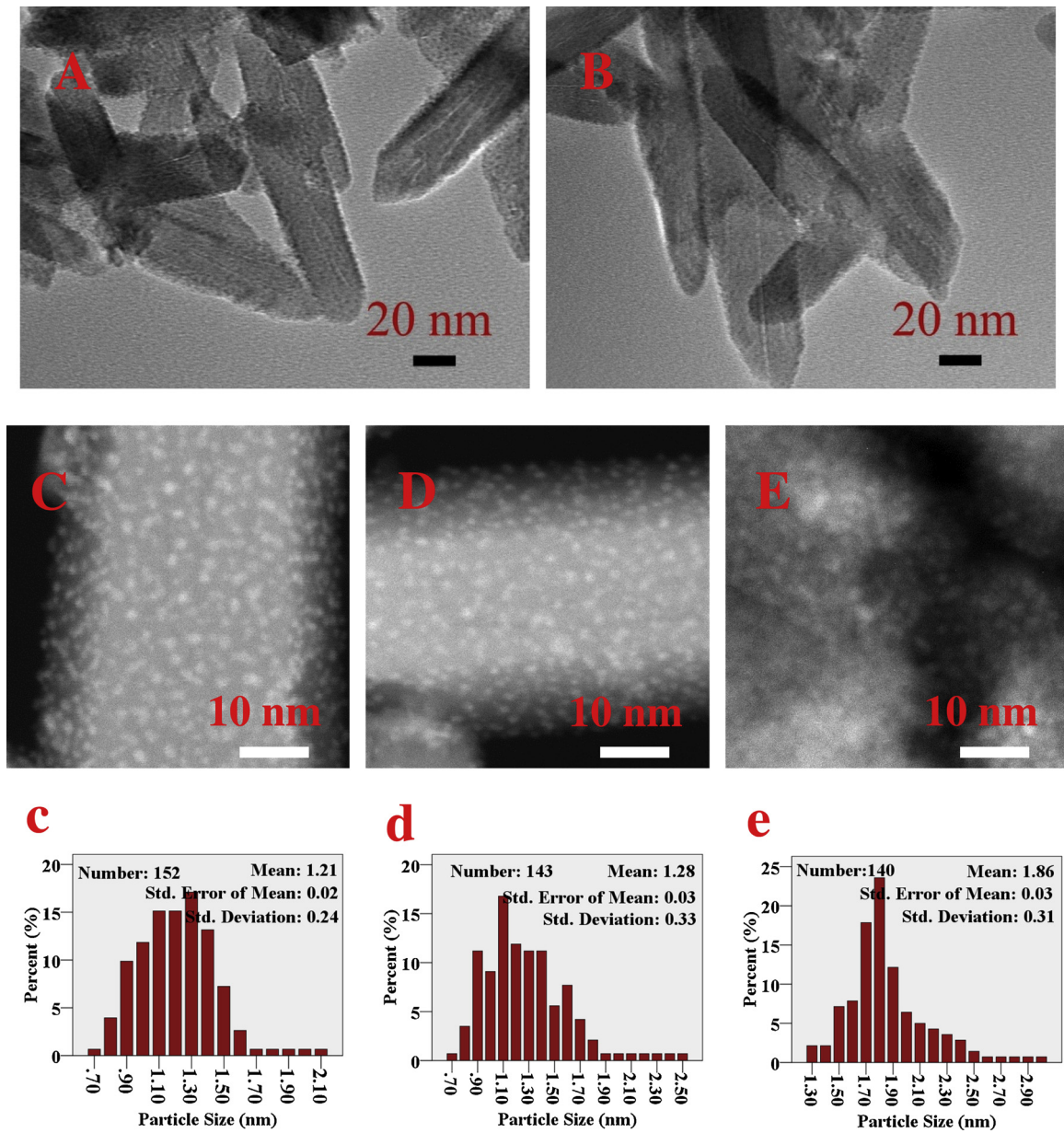


Fig. 5. TEM images of Pd/ST-2 (A and B); HAADF-STEM pictures of the catalysts. C. Pd/ST-2, D. Pd/ST(120)-2, E. Pd/T-2.

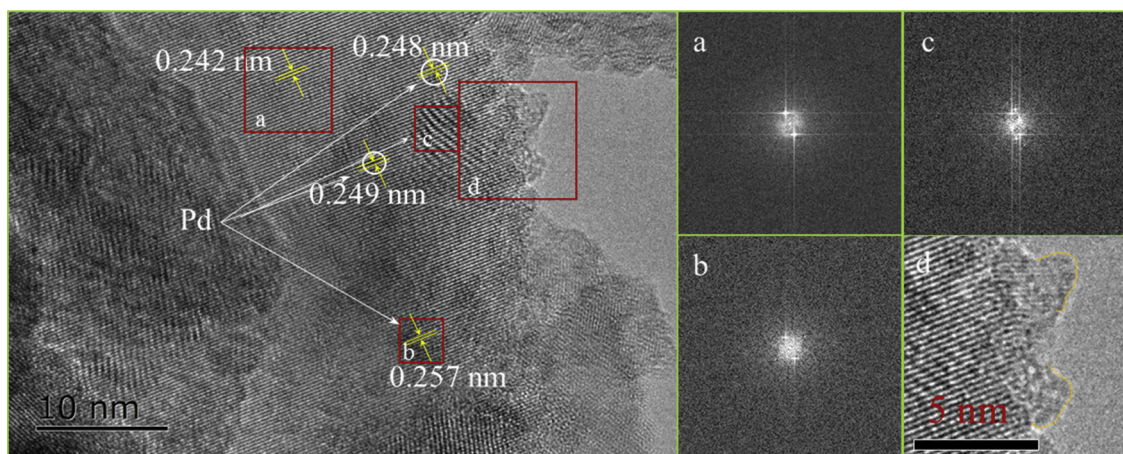


Fig. 6. HRTEM pictures of Pd/ST-2 (F).

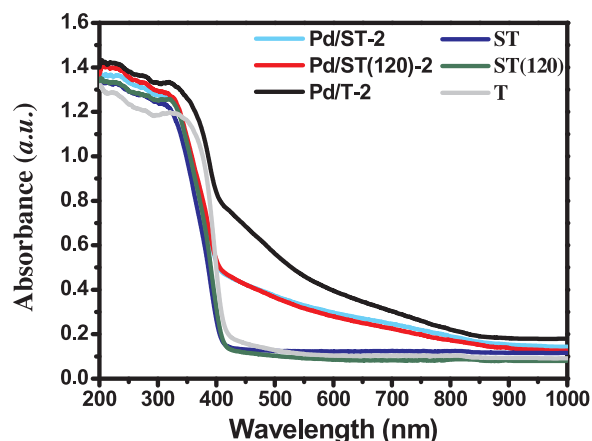


Fig. 7. UV-vis spectra of the samples ST, ST(120) and T with 2.0 wt.% Pd loading.

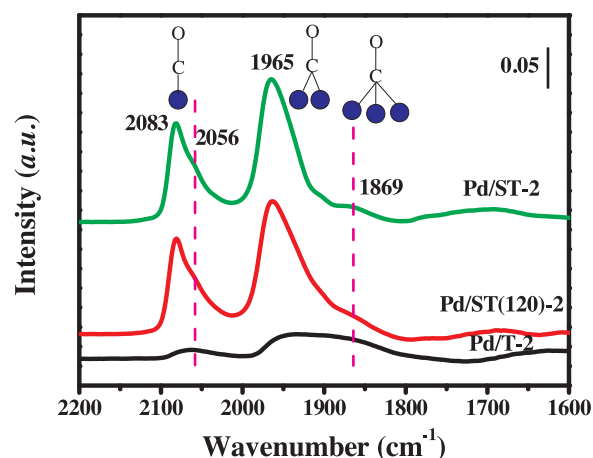


Fig. 9. CO DRIFT spectra of Pd based catalysts with the different supports.

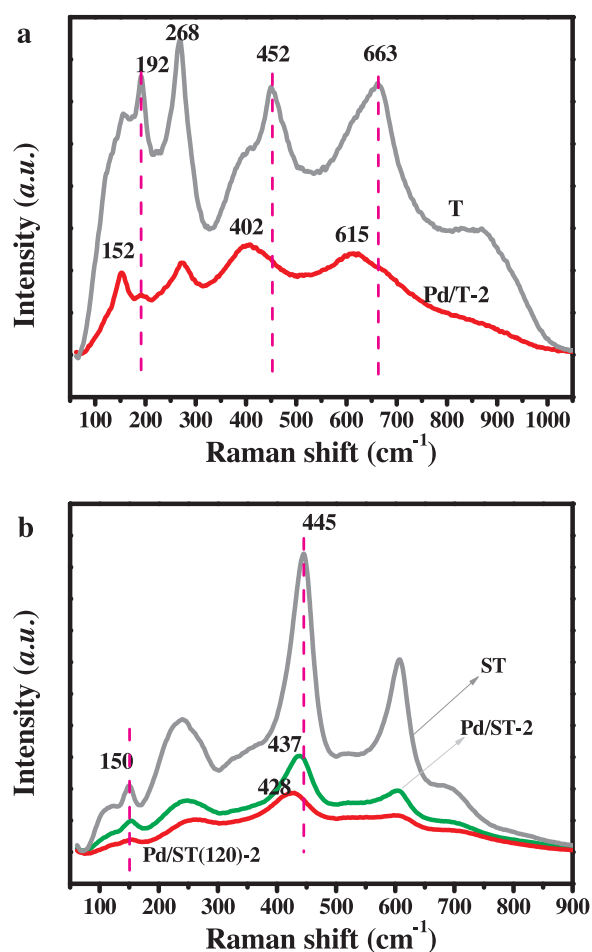


Fig. 8. Raman spectra of Pd based catalysts with the different supports.

The surface structure was further probed by CO-adsorbed IR technique. CO adsorption on Pd prefers the bridging or hollow sites much more than atop sites, whereby the geometric structures of Pd surfaces can be effectively probed. Fig. 9 exhibits the DRIFT spectra of CO adsorption on the catalysts Pd/ST-2, Pd/ST(120)-2 and Pd/T-2. For Pd/ST-2 catalyst, two main absorption bands centered at 1965 and 2083 cm<sup>-1</sup> were clearly distinguished. The former was stronger than the latter and could be assigned to CO adsorbed on 2-fold bridging sites, while the latter was broad with a shoulder and can be reasonably ascribed to CO linearly adsorbed on atop sites of Pd [54]. The presence of

the shoulder associated with the band 2083 cm<sup>-1</sup> implied that there were two types of atop sites on Pd nanoparticles [55]. A weak adsorption band at 1869 cm<sup>-1</sup> appeared, which could be assigned to the CO adsorbed on 3-fold hollow sites, indicating seldom presence of large Pd ensembles [54]. Pd/ST(120)-2 revealed similar peaks. The bands of Pd/T-2 shifted to low wavenumber which explained larger particles existed. The CO DRIFTS studies provided the evidence for the four active states of Pd on ST.

The H<sub>2</sub>-TPR patterns of ST and Pd/ST-2 presented in Fig. 10a. For ST supports, the H<sub>2</sub> consumption peaks occurred at high temperature

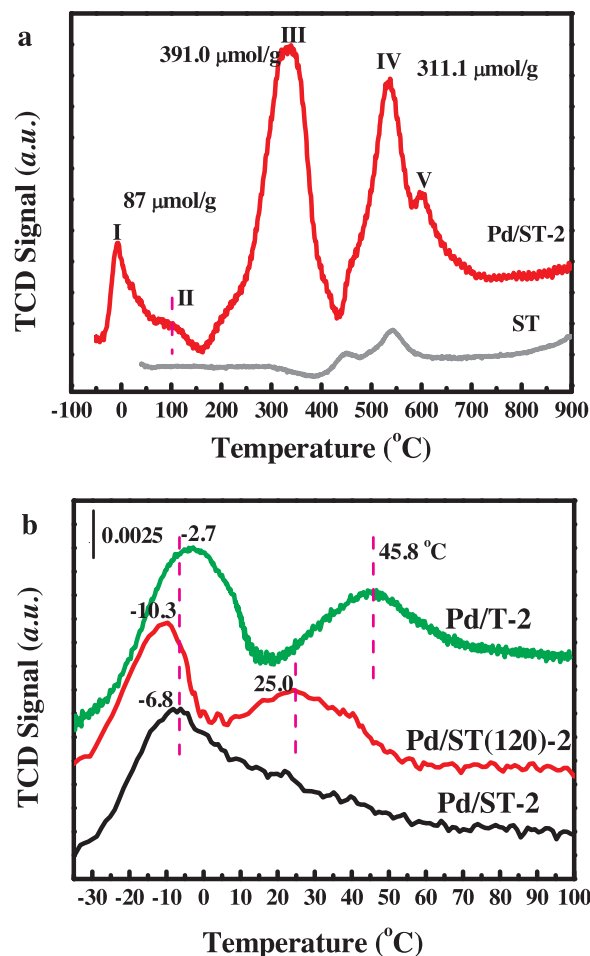


Fig. 10. H<sub>2</sub>-TPR profiles of Pd based catalysts with the different supports.

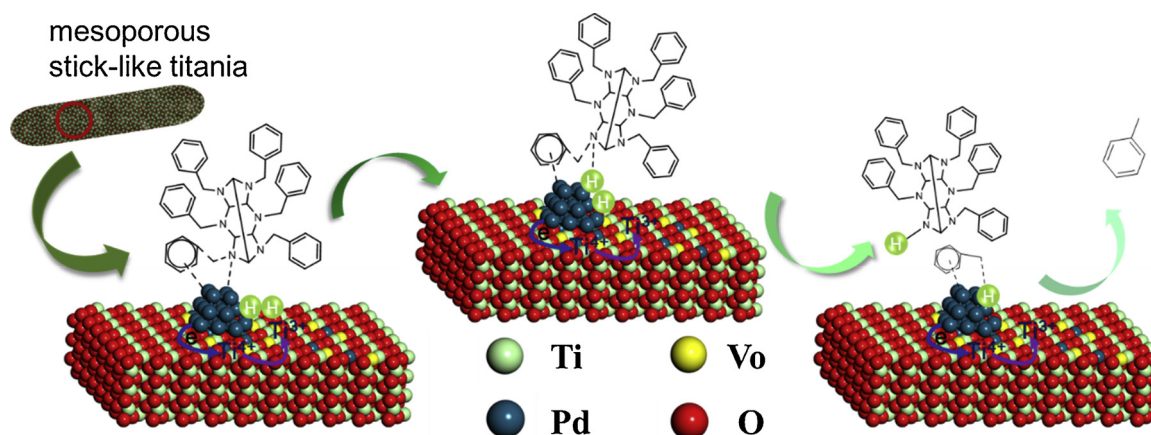


Fig. 11. Proposed catalytic mechanism of HBIW over Pd/ST-2.

449 °C and 542 °C, and attributed to the reduction of titania from  $\text{Ti}^{4+}$  to  $\text{Ti}^{3+}$  [51,53]. Two peaks may represent two types of titania. It is well known that the anatase titania is less thermodynamically and less structurally stable than rutile titania. On the basis of Raman spectra, it can be implied that the peak at 449 °C and 542 °C may be ascribed to that of anatase and rutile respectively. For Pd/ST-2 catalysts, an interesting observation that can be made here is five  $\text{H}_2$  consumption peaks appeared. It is generally accepted that fine bulk oxides of palladium are easily reduced to metallic palladium ( $\text{Pd}^0$ ) at low temperature. Combined with HAADF-STEM and CO DRIFT, the peak I at  $-7$  °C can be evidently ascribed to the reduction of ultrafine Pd nanoparticles, and the peak II at 100 °C associated with large particles in very small amount. The theoretical  $\text{H}_2$  consumption of Pd over Pd/ST-2 was  $187 \mu\text{mol/g}$ . The reduction of Pd oxides over Pd/ST-2 was incomplete with the consumption of the peak I and II together  $87 \mu\text{mol/g}$ . In the temperature range of 200 °C–700 °C, three  $\text{H}_2$  consumption peaks (III–V) was disclosed. It was reported that they may correspond to the reduction of palladium particles with various metal–support interactions [53]. Peak III was assigned to the reduction of titania in direct contact with Pd particles, Peak IV was attributed to the reduction of remote titania that was not in direct contact with the Pd particles, and Peak V was associated with the reduction of stable  $\text{PdO}$  species that were strongly interact with the titania support, or the reduction of well-dispersed  $\text{PdO}$  species on titania support, or the reduction of palladium–titanate species ( $\text{Pd}^{2+}$ -oxygen vacancy ( $\text{Vo}$ )- $\text{Ti}^{3+}$ ). For Pd/ST-2 catalyst, all three peaks emerged. Presence of metal sites would be favored to the reduction of titania. Compared with the unloaded titania, the reduction of titania in Pd/ST-2 catalysts can shift to lower temperatures. According to XRD, HRTEM and Raman, peak III–V could be assigned to the reduction of titania support in direct contact with Pd particles and without direct contact with Pd particles, and the reduction of palladium–titanate species ( $\text{Pd}^{n+}$ -oxygen vacancy ( $\text{Vo}$ )- $\text{Ti}^{3+}$ ). In the case of  $\text{H}_2$ -TPR, it was proved to form not only fine particles and strong interaction but also palladium–titanate species with  $\text{Pd}^{n+}$ -oxygen vacancy ( $\text{Vo}$ )- $\text{Ti}^{3+}$  over Pd/ST-2 as revealed by HRTEM, Raman and CO DRIFT. Similarly,  $\text{H}_2$ -TPR of Pd/ST(120)-2 and Pd/T-2 were tested and shown in Fig. 10b. It can be seen that the reduction were shifted to higher temperatures in the order of Pd/ST-2 < Pd/ST(120)-2 < Pd/T-2. The results were consistent with HAADF-STEM and CO DRIFT.

$\text{H}_2$  chemisorption amount of Pd based catalysts over the different supports are shown in Table 3. On the basis of the  $\text{H}_2$  pulse chemisorption, the dispersion of Pd can be calculated and are given in Table 3. It can be seen that the  $\text{H}_2$  chemisorption amount and dispersion of Pd increased by arrangement of the supports, T, ST(120) and ST. Combined with XRD, HRTEM, Raman and physical adsorption, the sample T formed microporous and amorphous crystal with  $\text{Ti}-\text{OH}$  on the surface of anatase and rutile phase, on the basis of which large Pd

particles accompanied with low dispersion can be observed. Rutile and seldom anatase phase and mesoporous structure with disturbed edges and tunnels surface appeared in the supports ST and ST(120), and then promoted Pd depositing into the interstices and lattice through the pH and strong interaction between metal salt and supports, which shaped ultrafine and even sub-nanometer Pd nanoparticles with high dispersion. The crystal structure of ST(120) supports matured with treatment temperatures increasing. Although the interaction and oxygen defects can be strengthened in the process of Pd depositing, Pd nanoparticles grew up on the smaller surface area of ST(120) and then exhibited lower dispersion than ST. In a word, the particle size of Pd over the supports followed the sequence: ST < ST(60) < ST(120) < T as proved by HAADF-STEM and UV-vis, and the dispersion was followed by Pd/ST-2 > Pd/ST(60)-2 > Pd/ST(120)-2 > Pd/T-2 according to  $\text{H}_2$  pulse chemisorption, which explained the catalytic performance of HBIW debenzoylation. Then the catalytic mechanism was proposed and is shown in the Fig. 11 on the basis of  $\text{H}_2$  pulse chemisorption, HRTEM, Raman and XPS. First, the ultrafine and even sub-nanometer Pd nanoparticles were highly dispersed over mesoporous stick-like ST. The electron-deficient Pd species ( $\text{Pd}^{n+}$ ) can be formed by the strong interaction and the palladium–titanate species ( $\text{Pd}^{n+}$ -oxygen vacancy ( $\text{Vo}$ )- $\text{Ti}^{3+}$ ) appeared, which can easily activate hydrogen. Second, the dispersed Pd improved the adsorption of HBIW. Third, the activated hydrogen attacked the bond of C–N from HBIW and finally, the hydrodebenzylation can be enhanced.

#### 4. Conclusions

Stick-like rutile titania with mesoporous were synthesized, on the basis of which highly efficient Pd based catalysts were developed for hydrodebenzylation of HBIW in this work. The preparation parameters played key roles on the textural and structural properties of the titania. The stick-like titania (ST) was received by low temperature treatment and showed large interplanar spacing, small average crystallite size and large mesoporous surface area. Pd can deposit into the interstices and lattice in the process of DP and then generated ultrafine and even sub-nanometer sizes with four kinds of states including palladium–titanate species ( $\text{Pd}^{n+}$ -oxygen vacancy ( $\text{Vo}$ )- $\text{Ti}^{3+}$ ), which were highly dispersed. Amorphous titania (T) obtained without Sr template showed blocky bulk with many irregular NPs and exhibited microporous and mesoporous structure and  $\text{Ti}-\text{OH}$  surface, meanwhile titania, ST(60) and ST(120), treated by high temperature formed matured crystal and mesoporous with small surface area. Then the particle size increased and the dispersion decreased for Pd catalysts over T, ST(60) and ST(120). Thus ST supported Pd catalysts with quite low loading 2 wt.% and Pd/HBIW usage 1‰ exhibited the highest TON in hydrodebenzylation of HBIW as compared to all the current reports and

commercial Pd/C catalysts, as well as Pd based catalysts with ST(60), ST(120) and T as supports.

### Declaration of Competing Interest

The authors declare that they have no conflict of interest.

### Acknowledgements

This work is financially supported by the National Natural Science Foundation of China (NO. 21503264 and 21503133), the Program for Professor of Special Appointment (Eastern Scholar) at Shanghai Institutions of Higher Learning, the Talent Program of Shanghai University of Engineering Science, Science and Technology Commission of Shanghai Municipality (18030501100), Shanghai Talent Development Foundation (2017076) and Natural Science Foundation of Hebei Province of China (B2017202182). The characterization is supported by Tao Zhang groups from Dalian Institute of Chemical Physics, Chinese Academy of Sciences.

### Appendix A. Supplementary data

Supplementary material related to this article can be found, in the online version, at doi:<https://doi.org/10.1016/j.mcat.2019.110556>.

### References

- [1] A. David, M.A. Vannice, Control of catalytic debenzoylation and dehalogenation reactions during liquid-phase reduction by H<sub>2</sub>, *J. Catal.* 237 (2006) 349–358.
- [2] C. Cheng, J. Sun, L. Xing, J. Xu, X. Wang, Y. Hu, Highly chemoselective Pd-C catalytic hydrodechlorination leading to the highly efficient N-debenzoylation of benzylamines, *J. Org. Chem.* 74 (2009) 5671–5674.
- [3] H.T. Hwang, J.R. Martinelli, R. Gounder, A. Varma, Kinetic study of Pd-catalyzed hydrogenation of N-benzyl-4-fluoroaniline, *Chem. Eng. J.* 288 (2016) 758–769.
- [4] M. Jose Albaladejo, M. Jose Gonzalez-Soria, F. Alonso, Synthesis of aminoindolizidines through the chemoselective and diastereoselective catalytic hydrogenation of Indolizines, *J. Org. Chem.* 81 (2016) 9707–9717.
- [5] R.C. Bernotas, R.V. Cube, The use of Pearlman's catalyst for selective N-debenzoylation in the presence of benzyl ethers, *Synth. Commun.* 20 (1990) 1209–1212.
- [6] M. Shokouhimehr, T. Kim, S.W. Jun, K. Shin, Y. Jang, B.H. Kim, J. Kim, T. Hyeon, Magnetically separable carbon nanocomposite catalysts for efficient nitroarene reduction and Suzuki reactions, *Appl. Catal. A* 476 (2014) 133–139.
- [7] K. Zhang, J.M. Suh, J.-W. Choi, H.W. Jang, M. Shokouhimehr, R.S. Varma, Recent advances in the nanocatalyst-assisted NaBH<sub>4</sub> reduction of nitroaromatics in water, *ACS Omega* 4 (2019) 483–495.
- [8] K. Zhang, K. Hong, J.M. Suh, T.H. Lee, O. Kwon, M. Shokouhimehr, H.W. Jang, Facile synthesis of monodispersed Pd nanocatalysts decorated on graphene oxide for reduction of nitroaromatics in aqueous solution, *Res. Chem. Intermed.* 45 (2019) 599–611.
- [9] M. Shokouhimehr, J.-H. Kim, Y.-S. Lee, Heterogeneous Heck reaction catalyzed by recyclable polymer-supported N-heterocyclic carbene-palladium complex, *Synlett* 2006 (2006) 0618–0620.
- [10] L. Ding, F. Zhao, Q. Pan, H. Xu, Research on the thermal decomposition behavior of NEPE propellant containing CL-20, *J. Anal. Appl. Pyrol.* 121 (2016) 121–127.
- [11] G. Hang, W. Yu, T. Wang, J. Wang, Z. Li, Theoretical insights into effects of molar ratios on stabilities, mechanical properties and detonation performance of CL-20/RDX cocrystal explosives by molecular dynamics simulation, *J. Mol. Struct.* 1141 (2017) 577–583.
- [12] A.T. Nielsen, A.P. Chafin, S.L. Christian, D.W. Moore, M.P. Nadler, R.A. Nissan, D.J. Vanderah, R.D. Gilardi, C.F. George, J.L. Flippen-Anderson, Synthesis of polyazapolycyclic caged polynitramines, *Tetrahedron* 54 (1998) 11793–11812.
- [13] H. Chen, S. Chen, S. Jin, L. Li, Improved debenzoylation of caged polycyclic amine hexabenzylhexaazaisowurtzitane, theory and practice of energetic materials, The 7th International Fall Seminar on Propellants, Explosives and Pyrotechnics, Oct 23–26, 2007 Vol VII (2007) 30–33 ed..
- [14] K. Dong, Y. Chen, Y. Zhang, C. Sun, S. Pang, The highly effective hydrogenolysis-based debenzoylation of tetraacetyl-dibenzyl-hexaazaisowurtzitane (TADBIW) using a Palladium/DOWEX catalyst having a synergistic effect, *J. Energy Mater.* 35 (2017) 421–429.
- [15] A.P. Koskin, I.L. Simakova, S.J. Troitskij, V.N. Parmon, Catalysts, method of its preparation and method of tetraacetyl-diformylhexaazaisowurtzitane preparation, (2009, Patent No.: RU2359753C1) 1–8.
- [16] Y. Bayat, H. Ebrahimi, F. Fotouhi, Optimization of reductive debenzoylation of hexabenzylhexaazaisowurtzitane (the key step for synthesis of HNIW) using response surface methodology, *Org. Process Res. Dev.* 16 (2012) 1733–1738.
- [17] C. Sun, Z.W. Feng, T. Fang, X.Q. Zhao, Synthesis and crystal structure of 2,6,8,12-tetraacetyl-2,4,6,8,10,12-hexaazatetracyclo[5.5.0.0<sup>5,9</sup>.0<sup>3,11</sup>]dodecane, *Chin. J. Struct. Chem.* 24 (2005) 204–208.
- [18] W. Qiu, H. Liu, K. Dong, C. Sun, S. Pang, G. Bai, X. Zuo, G. Zhang, H. He, Preparation of Pd(OH)<sub>2</sub>/C catalyst for hydrogenolytic debenzoylation of hexabenzylhexaazaisowurtzitane, *Chin. J. Energy Mater.* 22 (2014) 441–446.
- [19] P. Maksimowski, T. Golofit, W. Tomaszewski, Palladium catalyst in the HBIW hydrodebenzoylation reaction, deactivation and spent catalyst regeneration procedure, *Cent. Eur. J. Energy Mater.* 13 (2016) 333–348.
- [20] A.J. Bellamy, Reductive debenzoylation of hexabenzylhexaazaisowurtzitane, *Tetrahedron* 51 (1995) 4711–4722.
- [21] A.P. Koskin, I.L. Simakova, V.N. Parmon, Reductive debenzoylation of hexabenzylhexaazaisowurtzitane — the key step of the synthesis of polycyclic nitramine hexanitrohexaazaisowurtzitane, *Russ. Chem. Bull.* 56 (2007) 2370–2375.
- [22] F. Fotouhi-Far, H. Bashiri, M. Hamadani, Study of deactivation of Pd(OH)<sub>2</sub>/C catalyst in reductive debenzoylation of hexabenzylhexaazaisowurtzitane, *Propell. Explos. Pyrot.* 42 (2017) 213–219.
- [23] A.P. Koskin, I.L. Simakova, V.N. Parmon, Study of palladium catalyst deactivation in synthesis of 4,10-diformyl-2,6,8,12-tetraacetyl-2,4,6,8,10,12-hexaazaisowurtzitane, *React. Kinet. Catal. Lett.* 92 (2007) 293–302.
- [24] W. Han, Y. Ou, B. Chen, Investigation on hydrogenolysis of hexabenzylhexaazaisowurtzitane, *J. Beijing Inst. Technol.* 15 (2006) 225–228.
- [25] M. Zhang, S. Liu, L. Li, X. Li, H. Huang, J. Yin, X. Shao, J. Yang, Effect of carbon supports on Pd catalyst for hydrogenation debenzoylation of hexabenzylhexaazaisowurtzitane (HBIW), *J. Energy Mater.* 35 (2017) 251–264.
- [26] W. Hu, W. Zhou, K. Zhang, X. Zhang, L. Wang, B. Jiang, G. Tian, D. Zhao, H. Fu, Facile strategy for controllable synthesis of stable mesoporous black TiO<sub>2</sub> hollow spheres with efficient solar-driven photocatalytic hydrogen evolution, *J. Mater. Chem. A* 4 (2016) 7495–7502.
- [27] D. Banham, F.X. Feng, T. Furstenthaupt, K. Pei, S.Y. Ye, V. Birss, Novel mesoporous carbon supports for PEMFC catalysts, *Catalysts* 5 (2015) 1046–1067.
- [28] H. Alamgholiloo, S. Zhang, A. Ahadi, S. Rostamnia, R. Banaei, Z. Li, X. Liu, M. Shokouhimehr, Synthesis of bimetallic 4-PySI-Pd/Cu(BDC) via open metal site Cu-MOF: effect of metal and support of Pd@Cu-MOFs in H<sub>2</sub> generation from formic acid, *Mol. Catal.* 467 (2019) 30–37.
- [29] M. Shokouhimehr, M.S. Asl, B. Mazinani, Modulated large-pore mesoporous silica as an efficient base catalyst for the Henry reaction, *Res. Chem. Intermed.* 44 (2018) 1617–1626.
- [30] D.T. Nguyen, T. Charinpanitkul, D.W. Park, K.S. Kim, Preparation of magnetite hollow structure for drug delivery application, *J. Nanosci. Nanotechnol.* 14 (2014) 7995–7999.
- [31] S.W. Jun, M. Shokouhimehr, D.J. Lee, Y. Jang, J. Parka, T. Hyeon, One-pot synthesis of magnetically recyclable mesoporous silica supported acid-base catalysts for tandem reactions, *Chem. Commun.* 49 (2013) 7821–7823.
- [32] M. Shokouhimehr, J.E. Lee, S.I. Han, T. Hyeon, Magnetically recyclable hollow nanocomposite catalysts for heterogeneous reduction of nitroarenes and Suzuki reactions, *Chem. Commun.* 49 (2013) 4779–4781.
- [33] T.K. Vo, W.-S. Kim, S.-S. Kim, K.S. Yoo, J. Kim, Facile synthesis of Mo/Al<sub>2</sub>O<sub>3</sub>-TiO<sub>2</sub> catalysts using spray pyrolysis and their catalytic activity for hydrodeoxygenation, *Energy Convers. Manage.* 158 (2018) 92–102.
- [34] M. Park, B.S. Kwak, S.W. Jo, M. Kang, Effective CH<sub>4</sub> production from CO<sub>2</sub> photo-reduction using TiO<sub>2</sub>/x mol% Cu-TiO<sub>2</sub> double-layered films, *Energy Convers. Manage.* 103 (2015) 431–438.
- [35] A. Ahadi, S. Rostamnia, P. Panahi, L.D. Wilson, Q. Kong, Z. An, M. Shokouhimehr, Palladium comprising dicationic bipyridinium supported periodic mesoporous organosilica (PMO): Pd@Bipy-PMO as an efficient hybrid catalyst for suzuki-miyaura cross-coupling reaction in water, *Catalysts* 9 (2019) 140.
- [36] A. Kim, S.M. Rafiaei, S. Abolhosseini, M. Shokouhimehr, Palladium nanocatalysts confined in mesoporous silica for heterogeneous reduction of nitroaromatics, *Energy Environ. Focus* 4 (2015) 18–23.
- [37] M. Shokouhimehr, Y. Piao, J. Kim, Y. Jang, T. Hyeon, A magnetically recyclable nanocomposite catalyst for olefin epoxidation, *Angew. Chem. Int. Ed.* 46 (2007) 7039–7043.
- [38] M. Shokouhimehr, K. Hong, T.H. Lee, C.W. Moon, S.P. Hong, K.Q. Zhang, J.M. Suh, K.S. Choi, R.S. Varma, H.W. Jang, Magnetically retrievable nanocomposite adorned with Pd nanocatalysts: efficient reduction of nitroaromatics in aqueous media, *Green Chem.* 20 (2018) 3809–3817.
- [39] M. Shokouhimehr, K.Y. Shin, J.S. Lee, M.J. Hackett, S.W. Jun, M.H. Oh, J. Jang, T. Hyeon, Magnetically recyclable core-shell nanocatalysts for efficient heterogeneous oxidation of alcohols, *J. Mater. Chem. A* 2 (2014) 7593–7599.
- [40] K.H. Choi, M. Shokouhimehr, Y.E. Sung, Heterogeneous Suzuki cross-coupling reaction catalyzed by magnetically recyclable nanocatalyst, *Bull. Korean Chem. Soc.* 34 (2013) 1477–1480.
- [41] D. Lou, H. Wang, S. Liu, L. Li, W. Zhao, X. Chen, J. Wang, X. Li, P. Wu, J. Yang, PdFe bimetallic catalysts for debenzoylation of hexabenzylhexaazaisowurtzitane (HBIW) and tetraacetyldibenzylhexaazaisowurtzitane (TADBIW), *Catal. Commun.* 109 (2018) 28–32.
- [42] S. Nong, W. Dong, J. Yin, B. Dong, Y. Lu, X. Yuan, X. Wang, K. Bu, M. Chen, S. Jiang, L.-M. Liu, M. Sui, F. Huang, Well-dispersed ruthenium in mesoporous crystal TiO<sub>2</sub> as an advanced electrocatalyst for hydrogen evolution reaction, *J. Am. Chem. Soc.* 140 (2018) 5719–5727.
- [43] J.C. Parker, R.W. Siegel, Calibration of the Raman spectrum to the oxygen stoichiometry of nanophase TiO<sub>2</sub>, *Appl. Phys. Lett.* 57 (1990) 943–945.
- [44] H. Sutiono, A.M. Tripathi, H. Chen, C. Chen, W. Su, L. Chen, H. Dai, B. Hwang, Facile synthesis of [101]-oriented rutile TiO<sub>2</sub> nanorod array on FTO substrate with a tunable anatase–rutile heterojunction for efficient solar water splitting, *ACS Sustain. Chem. Eng.* 4 (2016) 5963–5971.
- [45] K. Vijayarangamuthu, J.S. Youn, C.M. Park, K.J. Jeon, Facile synthesis of core-shell-

- structured rutile TiO<sub>2</sub> with enhanced photocatalytic properties, *Catal. Today* (2018), <https://doi.org/10.1016/j.cattod.2018.1005.1038>.
- [46] Y. Zhang, C.X. Harris, P. Wallenmeyer, J. Murowchick, X. Chen, Asymmetric lattice vibrational characteristics of rutile TiO<sub>2</sub> as revealed by laser power dependent raman spectroscopy, *J. Phys. Chem. C* 117 (2013) 24015–24022.
- [47] R. Shannon, Revised effective ionic radii and systematic studies of interatomic distances in halides and chalcogenides, *Acta Crystallogr. A* 32 (1976) 751–767.
- [48] D.S. Garcia-Zaleta, A.M. Torres-Huerta, M.A. Dominguez-Crespo, A. Garcia-Murillo, R. Silva-Rodrigo, R.L. Gonzalez, Influence of phases content on Pt/TiO<sub>2</sub>, Pd/TiO<sub>2</sub> catalysts for degradation of 4-chlorophenol at room temperature, *J. Nanomater.* 2016 (2016) 1–15.
- [49] X. Zhang, H. Gao, X. Li, Atomistic simulations of superplasticity and amorphization of nanocrystalline anatase TiO<sub>2</sub>, *Extreme Mech. Lett.* 22 (2018) 131–137.
- [50] G. Okeke, R.B. Hammond, S.J. Antony, Effects of heat treatment on the atomic structure and surface energy of rutile and anatase TiO<sub>2</sub> nanoparticles under vacuum and water environments, *Chem. Eng. Sci.* 146 (2016) 144–158.
- [51] N.S. Babu, N. Lingaiah, N. Pasha, J.V. Kumar, P.S.S. Prasad, Influence of particle size and nature of Pd species on the hydrodechlorination of chloroaromatics: studies on Pd/TiO<sub>2</sub> catalysts in chlorobenzene conversion, *Catal. Today* 141 (2009) 120–124.
- [52] C. Langhammer, Z. Yuan, I. Zorić, B. Kasemo, Plasmonic properties of supported Pt and Pd nanostructures, *Nano Lett.* 6 (2006) 833–838.
- [53] T. Hengsawad, T. Jindarat, D.E. Resasco, S. Jongpatiwut, Synergistic effect of oxygen vacancies and highly dispersed Pd nanoparticles over Pd-loaded TiO<sub>2</sub> prepared by a single-step sol–gel process for deoxygenation of triglycerides, *Appl. Catal. A Gen.* 566 (2018) 74–86.
- [54] P. Tian, L. Ouyang, X. Xu, C. Ao, X. Xu, R. Si, X. Shen, M. Lin, J. Xu, Y. Han, The origin of palladium particle size effects in the direct synthesis of H<sub>2</sub>O<sub>2</sub>: is smaller better? *J. Catal.* 349 (2017) 30–40.
- [55] L. Zhang, A. Wang, J.T. Miller, X. Liu, X. Yang, W. Wang, L. Li, Y. Huang, C. Mou, T. Zhang, Efficient and durable Au alloyed Pd single-atom catalyst for the Ullmann reaction of aryl chlorides in water, *ACS Catal.* 4 (2014) 1546–1553.